Journal of Structural Geology 30 (2008) 876–887

Contents lists available at ScienceDirect

Journal of Structural Geology

journal homepage: www.elsevier.com/locate/jsg

High-resolution tomography of cracks, voids and micro-structure in greywacke and limestone

S. Zabler [a,*], A. Rack [a,1], I. Manke [a], K. Thermann [b], J. Tiedemann [b], N. Harthill [c], H. Riesemeier [d]

[a] Hahn-Meitner-Institute Berlin, Materials dpt. SF3, Glienicker Str. 100, 14109 Berlin, Germany
[b] Technical University Berlin, Engineering Geology, Ackerstr. 76, 13355 Berlin, Germany
[c] University of Karlsruhe, Geophysics Institute, Hertzstraße 16, 76187 Karlsruhe, Germany
[d] Bundesanstalt für Materialforschung und -prüfung (BAM), Unter den Eichen 87, 12205 Berlin, Germany

ARTICLE INFO

Article history:
Received 11 July 2006
Received in revised form 21 February 2008
Accepted 4 March 2008
Available online 12 March 2008

Keywords:
Rock porosity
Crack formation
X-ray imaging
Micro-tomography
3D image analysis

ABSTRACT

Rocks are commonly very heterogeneous materials. Randomly distributed micro-flaws inside the rock are believed to initiate tensile cracks from which shear fractures develop and coalescence through en echelon interactions leads to fracture. In this paper, we describe the results of applying high-resolution X-ray tomography to samples of greywacke and limestone experimentally deformed under unconfined axial shortening at various loads equivalent to different fractions of the sample strength. Mineral grains, pores, micro-cracks and other voids were imaged with a resolution of 10 μm. 3D image analysis enabled us to monitor the initial state of the samples and the changes in them due to compression. Crack morphology is characterized and compared to the micro-structure of the sample before and after deformation. In the greywacke, formation of a macro-crack ~10° oblique to the stress direction is observed. It initiated in fine intergranular material at the top tip of the sample and is composed of tensile fractures connected by wing cracks. None of the voids defined in the initial state fractured, and the crack is interpreted to have started either as a micro-crack which was smaller than the resolution of the tomography, or, as a completely new crack. In the limestone, cracks are observed to initiate in features that are too small to be imaged by the tomography, or also in newly created cracks.

1. Introduction

The aim of this work was to obtain knowledge about the formation and propagation of cracks in natural rocks through the use of modern high-resolution X-ray computed tomography (CT). X-ray CT is non-destructive with – in this work – the capability of imaging details down to 10 μm. Most importantly, the internal structure and composition of rocks can be imaged before and after stress is applied to determine where and how cracks initiated. The study of fracture mechanics began when Griffith (1920, 1924) developed his "Theory of Rupture" and showed, both theoretically and experimentally, that the location of rupture in materials is due to the presence of flaws. In Griffith's experiments, these flaws were notches created in glass rods which were then subjected to tensional stress. Later, McClintock and Walsh (1962) extended Griffith's theory to compressive stresses. For a discussion of Griffith's work and linear elastic fracture mechanics in general, see, e.g., Scholz (1990, 2002). In rocks, flaws may occur down to the atomic lattice scale and descriptions of the existence of micro-flaws in rocks are rare because of the lack of non-destructive methods with sufficient resolving power, i.e., on the micrometer scale. Due to their strongly heterogeneous nature, experimental and analytical characterization of the elastic properties and fracture strength of rocks is not very reproducible. In other words, the bulk behavior of many rocks under stress is controlled by the local distribution of flaws, fossils, inclusions, cavities, grain boundaries, mineral cleavage planes and micro-cracks. In addition, in the case of monomineralic and some crystalline rocks, the flaws may not be apparent until stress is applied. In order to better understand the process which leads from micro-cracks to macroscopic fracturing – which extends in scale from millimeters to kilometers – crack initiation, propagation and growth should be studied on the micrometer scale. In this paper, the generic term void will be used to describe pre-existing flaws, pores and cracks, etc (cf. Kranz, 1983).

Cracks are three-dimensional surfaces, yet most microscopic investigations on fracturing in rocks have been limited to the analysis of thin sections (e.g. Janssen et al., 2001; Moore and Lockner, 1995) with subsequent interpretation of the 2D results to gain a 3D image. An alternative technique is the monitoring of acoustic emissions (AE) from cracks propagating during

* Corresponding author. Max-Planck Institute of Colloids and Interfaces, 14476 Potsdam-Golm, Germany. Tel.: +49 331 567 9453; fax: +49 331 567 9402.
E-mail address: simon.zabler@mpikg.mpg.de (S. Zabler).
[1] Current address: Forschungzentrum Karlsruhe, ANKA - Institute for Synchrotron Radiation, 76344 Eggenstein-Leopoldshafen, Germany.

0191-8141/$ – see front matter © 2008 Elsevier Ltd. All rights reserved.
doi:10.1016/j.jsg.2008.03.002

experiments. This technique can clearly show the nucleation of fractures in a 3D image of the hypocenters as well as crack progression through the sample (e.g. Lei et al., 2000; Reches and Lockner, 1994; Zang et al., 2000) but does not define the microcrack before stress is applied. The first 3D images of propagating cracks were obtained from materials that are transparent to visible light. Numerous investigations on the fracturing of glass (e.g. Bieniawski, 1967; Germanovich et al., 1994; Hoek and Bieniawski, 1965), resin (e.g. poly-methyl-meta-acrylate; Dyskin et al., 1995; Dyskin et al., 2003; Horii and Nemat-Nasser, 1985; Cannon et al., 1990) and ice (Schulson et al., 1999) were reported. These transparent materials permit the fracture process to be studied while controlling the concentration of *ab initio* defects in the samples. Cross-sectional images of fractured gypsum samples were studied extensively by Bobet and Einstein (1998) and Lajtai (1971, 1974).

With X-ray tubes becoming a standard tool in geophysical laboratories the amount of research on the three-dimensional distribution of grains and voids in natural rock has increased significantly over the last ten years (Hirono et al., 2003; Ketcham, 2005; Ohtani et al., 2001; Vervoort et al., 2003). In addition to natural rocks, X-ray computed tomography (CT) was applied to study many "rock-like" materials such as mortar and concrete (Landis et al., 2003; Otani and Obara, 2003). As the number of studies increased, so did the highest available resolution of the method (e.g. Desrues et al., 2006). X-ray CT was shown to be particularly useful for the analysis of the hierarchical size distribution of voids and minerals in rocks because this technique has the potential to visualize details ranging over many orders of magnitude, e.g., from 0.5 μm to 0.5 m. The number of reports on 3D imaging of natural rock whereby mineral phases as well as micro-cracks were analyzed, increased with the availability of neutron radiography and tomography using cold and/or thermal neutron sources (Bastuerk et al., 2004; Lunati et al., 2003; Winkler et al., 2002). Typical rock-forming minerals (e.g., quartz, feldspars, micas, pyroxenes, amphiboles) are highly transparent to neutrons, which allow for recording of projection images of relatively large samples (1–10 cm). However, the maximum spatial resolution of neutron tomography (100 μm) is not capable of imaging the very small void spaces known to be inherent to natural rocks (Fredrich et al., 1995). Similarly the resolving power of X-ray tomography is limited to some tenths of a millimeter in most cases. Therefore 3D imaging of the mineral and crack distribution in rock with micrometer details was restricted to the users of hard X-ray beamlines, where wavelengths from 0.5 nm to 0.02 nm are typically available. Reports on these imaging experiments, with a resolution ranging from 10 to 20 μm are still rare (Bésuelle et al., 2006; Landis, 2006; Lenoir et al., 2003; Matsushima et al., 2003; Nakashima et al., 2004). Samples with dimensions of 1 mm can be analyzed with the best reported resolution in the sub-micrometer range. For this work we used a setup with a spatial resolution of ~10 μm and capable of imaging voids and minerals in 6–7 mm sized samples. Two types of sedimentary rock were chosen to represent heterogeneous and homogeneous sedimentary rocks and are: a Carboniferous greywacke with a heterogeneous distribution of various minerals and grain sizes, and a Triassic limestone with a very homogeneous fine-grained micro-structure. The results of this study, by comparing the sample structure before and after compression will determine the effect of pre-existing voids on the fracturing sequence.

2. Materials

The greywacke that was used for the present work comes from a core hole near Waldeck and the limestone from the vicinity of Berlin, both in Germany. Fig. 1 shows two microscopic images of thin sections of the two investigated rocks. The cutting plane was chosen so that the direction of maximum compression (applied to

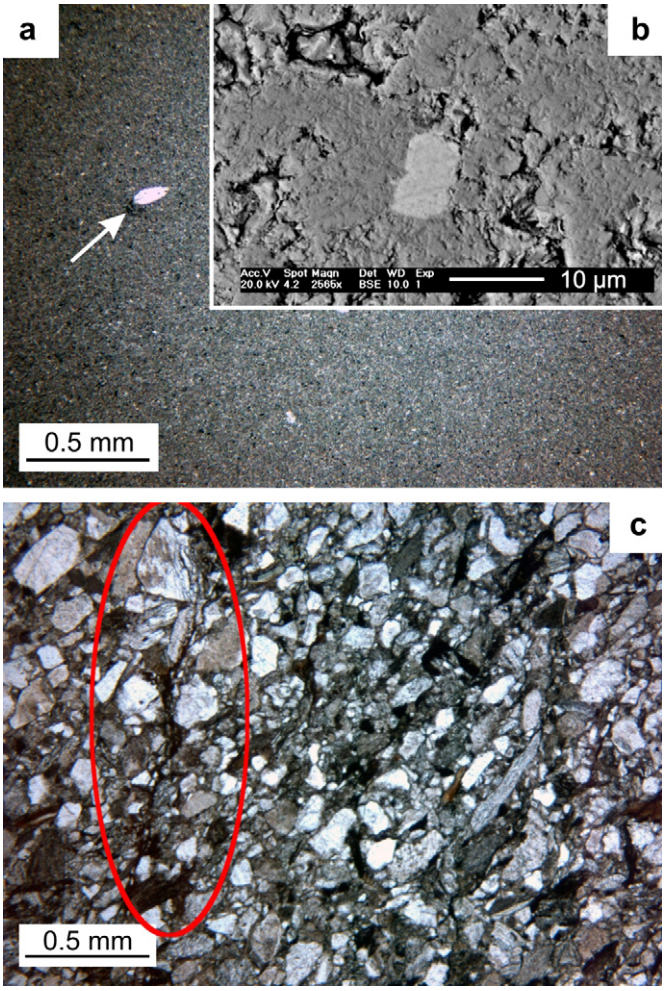

Fig. 1. (a) Microscopy of a cross-sections of limestone (the arrow indicates a sparitic shell included in the fine clay-matrix). The inset (b) shows a magnified scanning (backscattered) electron microscopy image of the same limestone revealing micrometer-sized inter-granular porosity and pyrites (bright contrast) of ca. 10 μm size. (c) Microscopy image of greywacke showing various mineral grains of different sizes (quartz, feldspar and biotites) ranging from 10 μm to 0.5 mm. An old "healed" crack that is filled with (opaque) ore minerals is indicated by the red ellipse.

cylindrical samples of the same material) would lie in the plane. The limestone may be classified as a micrite. During SEM measurements we observed an average grain size smaller than 5 μm and few sparitic shells. The inset (Fig. 1b) shows an electron microscope image of the fine limestone grains revealing micrometer-sized inter-granular porosity. Energy dispersive X-ray analysis further revealed that small pyrites are randomly distributed through the fine limestone matrix (e.g. the bright grain in Fig. 1b). The greywacke consists of angular and rounded grains of polycrystalline quartz and rock fragments of igneous origin embedded in a compact, fine grained matrix. Grain sizes of the mineral constituents range from 10 μm to 0.5 mm. An EDX analysis of the greywacke shows that the greywacke is composed of ~40% quartz, ~40% plagioclase, ~10% biotite and iron oxides, ~5% calcite, and 5% other. The presence of the plagioclase and biotite may have the effect of initiating cracking through cleavage. Consequently the coarse-grained greywacke should have a completely different fracture behavior compared to the limestone. Unlike the latter, the greywacke is characterized by a preexisting anisotropy observed through "healed" cracks which are filled with opaque iron oxides (e.g. see the ellipse in Fig. 1c). Such healed cracks indicate that the greywacke had been fractured and the resulting cavities were filled with ore minerals.

Preparation of the samples for deformation and micro-tomography was relatively simple. For each rock type small cylinders of approximately 6.6 mm in diameter and 10 mm height were drilled out of the bulk material. In order to obtain reproducible results samples of greywacke were cut so that the long cylinder axis had a defined orientation ($\sim 30^\circ$) with respect to the healed cracks. The small cylinder size was chosen to allow the samples to fit into the field of view of the detector array and, at the same time, to allow visualization of details of a size of at least 10 μm. Larger samples would require X-rays of higher energies (i.e., $E > 100$ keV) in order to guarantee a sufficient translucency. Such energies were not available in the present case which is why the sample diameter was limited to less than 7 mm.

3. Experiments

Monochromatic X-ray tomography was chosen because it is free of imaging artifacts that are inherent in polychromatic laboratory CT (beam hardening effects). A high-resolution 3D data volume representing the sample is reconstructed from 900 projection images recorded over 180 degrees (i.e., images are recorded at 0.2° intervals) for each sample. The time to take a tomogram is approximately 1 h (Appendix A). To begin with, we compressed six test cylinders of each rock until fracture occurred in order to determine the average compressive strength (stress) $\langle\sigma_{max}\rangle$ and strain (failure) $\langle\varepsilon_{max}\rangle$; the stress and strain measurements are integrated into the testing machine. Then, three new cylinders of each material were selected and complete tomograms were acquired of their initial micro-structure. Subsequently, each sample was axially loaded to a specific percentage of the average maximum strain $\langle\varepsilon_{max}\rangle$: 60% (samples G1, and L1), 80% (samples G2 and L2) and 90% (sample G3 and L3). Strain-controlled uniaxial compression was applied at constant speed (0.1 mm/min) to the dry samples that were placed between the two loading plates of a universal compression device (UP25) without any additional confining pressure. After compression the samples were unloaded and repositioned on the tomography stage where a second 3D image of every sample was taken. Note: because the tomograms were recorded after unloading, the observed fracture includes effects which are due to stress release. The measured stress–strain curves for limestone and greywacke are shown in Fig. 2a and b along with photos of a fractured sample of each material. Whilst all limestone samples split in many columns, for the greywacke a single fracture developed, sometimes sub-parallel, sometimes oblique to the direction of the applied stress dividing the sample into two pieces. The fracture shown in Fig. 2b is oriented about 30° to the long cylinder axis which is parallel to the shortening direction. Such a behavior is quite uncommon and can be attributed to the preexisting anisotropy in the greywacke. The large fracture seen in Fig. 2b developed more or less parallel to "healed" cracks whereas a smaller crack (right hand side of the sample) aligns with the long sample axis indicating that two different mechanisms control the fracturing in greywacke. The results on the average maximum strain $\langle\varepsilon_{max}\rangle$ are indicated in the graphs by vertical dotted lines and the scatter of these values is marked by the grey bars in Fig. 2. The deformed samples had a length-to-diameter ratio in the range of 1.4–1.7. We corrected the measured average maximum strain and strength for the different ratios by using the shape correction given in Pells (1993). For greywacke we obtained $\langle\sigma_{max}\rangle \approx 74 \pm 10$ MPa (mean value ± standard deviation) and for limestone $\langle\sigma_{max}\rangle \approx 87 \pm 26$ MPa. These values are slightly lower than those given in Pells (1993) (greywacke, mean value 81 MPa; limestone, mean value 105 MPa). As can be seen from the stress–strain curves the scattering of the σ_{max} values was very pronounced in particular for the limestone samples. This result contradicts the behavior that would be expected from the fine homogeneous micro-structure. Hence

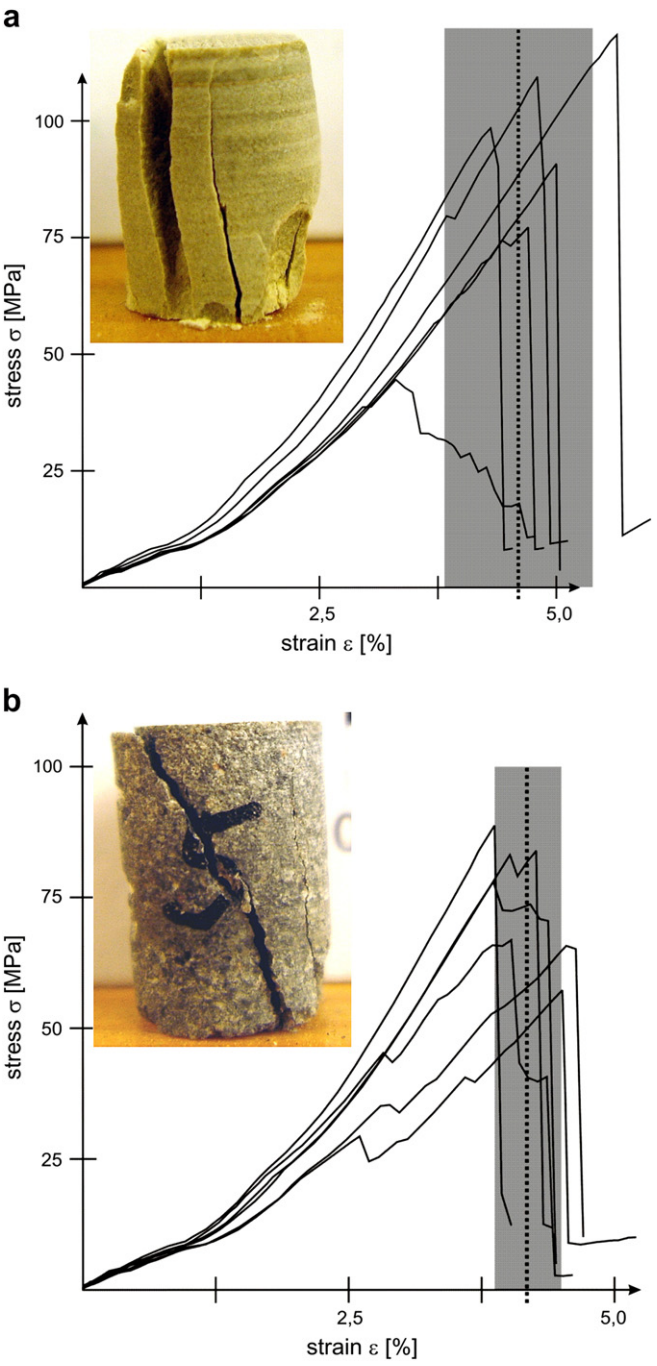

Fig. 2. Stress–strain curves obtained from fracture tests on small cylinders of (a) limestone and (b) greywacke. The dashed lines indicate the average compressive strength and the grey bars mark the scattering of the individual values. The insets show photos of fractured greywacke and limestone samples. Note the multi-columnar fracture of the limestone in contrast to the single oblique fracture of the greywacke.

inclusions (e.g., sparitic shells as seen in Fig. 1c) may be responsible for the large variation in material strength. Some deformation curves show non-linear "kinks" prior to peak stress indicating partial relaxation due to the formation of cracks or collapse of voids inside the samples. Alternatively, these kinks might be related to irregularities in the sample shape. From Fig. 2 it is also seen that the values of maximum strain $\langle\varepsilon_{max}\rangle$ scatter less than the compressive strength. The tests on limestone yielded $\langle\varepsilon_{max}\rangle \sim 4.6 \pm 0.7\%$, whereas the greywacke samples attained $\langle\varepsilon_{max}\rangle \sim 4.17 \pm 0.2\%$.

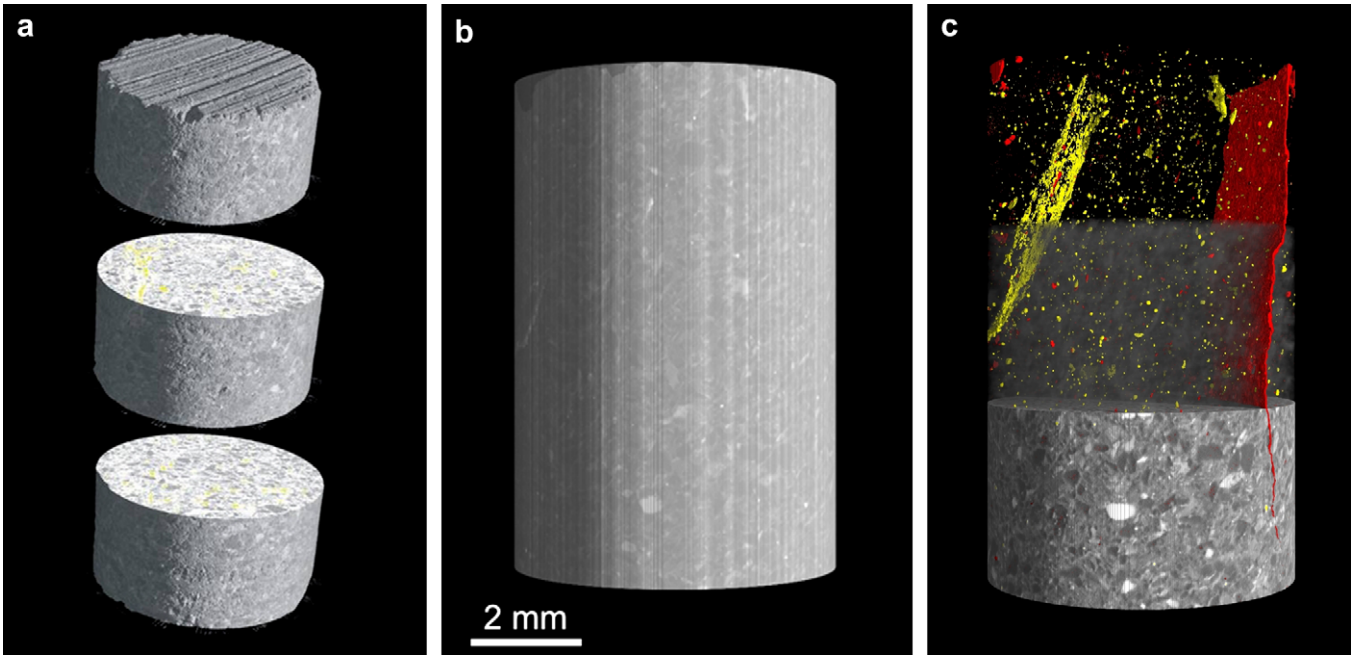

Fig. 3. 3D images of the sample G3: (a) virtual assembly of three tomograms of G3 that were recorded to map the entire height of the sample. (b) $2 \times 2 \times 2$ binning is applied to the complete dataset which is further converted into 8-bit data in order to reduce the computer memory required for image analysis. (c) Reconstruction of linear absorption coefficients allows grains and phases in the greywacke to be distinguished. In red, porosity and a macro-crack forming after strong deformation; in yellow, dense mineral particles reveal a "healed" crack ca. 30° inclined to the shortening direction.

4. Data processing

Following data acquisition, 3D images were reconstructed using the open-source software PyHST[2] and saved as raw volumes with 8-bit resolution. Because of the limited vertical dimension of the X-ray beam, three tomograms were recorded at different heights to cover the entire sample volume. In a first step these three recorded sections are assembled into one dataset; Fig. 3a and 3b depict how the different parts of sample G3 are aligned. In Fig. 3c, the different micro-structural components are illustrated by coloring cracks and ore minerals and setting low density minerals transparent. The total analyzed volume per sample was 0.5 mm^3, representing a three-dimensional space of $2037 \times 2037 \times 2500$ voxels (volumetric pixels). For some parts of the image analysis, $2 \times 2 \times 2$ binning was applied to the 3D data in order to reduce the number of voxels by a factor of 8 without compromising information that is required for the analysis. X-ray tomography measures the 3D distribution of the linear attenuation coefficient by assigning different gray values to different material phases in the image. We can therefore not only distinguish void spaces from bulk material but also different minerals within the sample (see the lower part of Fig. 3c).

5. Results

Tomographic records were taken of three limestone (L1–3) and greywacke (G1–3) samples before and after deformation which reached 60%, 80% and 90% of the average maximum strain $\langle \varepsilon_{max} \rangle$ (cf. Fig. 2). 3D image analysis (cf. Appendix B) was applied to characterize the porosity $n = V_{void}/V_{total}$ and void density N (voids per mm^3 sample volume) for each record. The results are listed in Table 1. For the greywacke application of 60% average maximum strain resulted in a decrease of porosity (G1: $(n_{loaded} - n_{initial})/n_{initial} = -28\%$). (Note that the pore density in the undeformed sample G1 was corrupted by strong image noise and is therefore not shown in Table 1. Filtering the smallest particles that were presumably the artifacts of this noise did not change porosity significantly allowing for a lower estimate of n whereas the number of voids changed drastically and is no longer comparable to the other samples. We assume the uncertainty for the void values in the other datasets to be smaller than one-fifth of the values given in Table 1). For 80% strain the void volume in G2 increased slightly: $(n_{loaded} - n_{initial})/n_{initial} = +3\%$, whereas a larger increase is observed for the void density in the same sample: $(N_{loaded} - N_{initial})/N_{initial} = +40\%$. The deformation picture changes entirely when 90% deformation is applied to sample G3 and we find a strong increase in total void volume ($\Delta n/n_{initial} = +1028\%$) which is related to the formation of a "macroscopic" crack shown in red in Fig. 3c. Also shown in Fig. 3c is a "healed" crack filled with iron oxide minerals (yellow). Note that the new crack did not exactly develop sub-parallel to the healed crack which is more similarly oriented to the main fracture in Fig. 2b (30° with respect to the shortening direction). Void density decreases after compression of G3 by $\Delta N/N_{initial} = -44\%$. For the limestone a strong increase in both void volume (L1: $\Delta n/n_{initial} = +52\%$; L2: $\Delta n/n_{initial} = +75\%$) and void density (L1: $\Delta N/N_{initial} = +50\%$; L2: $\Delta N/N_{initial} = +48\%$) is observed after compression to 60% and 80% of $\langle \varepsilon_{max} \rangle$. In the 3D image of L2, micro-cracks form explaining at least part of the increase in void volume. For sample L3, the increase of void volume ($\Delta n/n_{initial} = +500\%$) is not as large as in G3 but still significant due to the formation of micro-cracks (cf. Fig. 4). In contrast to G3, cracking of L3 is accompanied by a simultaneous increase in void density: $\Delta N/N_{initial} = +509\%$.

To refine our observations of void volume and void density we proceeded by calculating the distributions of shape and size of the individual voids in the uncompressed greywacke sample G2 and limestone sample L2.[3] Fig. 5a–d shows histograms of void volume

[2] Contact Dr A. Mirone: SciSoft Group of the European Synchrotron Facility (http://www.esrf.eu).

[3] 3D image analysis was performed using the software package MAVI (Modular Algorithms for Volume Images) distributed by the Fraunhofer Institute for Industrial Mathematics (ITWM) Kaiserslautern, Germany; contact: Dr K. Schladitz, schlad@itwm.fhg.de.

Table 1
Sample G3: void space n calculated by means of 3D image analysis of the deformed and the undeformed samples of greywacke (G1–3) and limestone (G1–3)

Sample	Analyzed volume (mm^3) ($x \times y \times z$)	Strain (%)	Stress (MPa)	Initial porosity n (‰)	Final porosity n (‰)	N_{pores} per mm^3 before deformation	N_{pores} after application of stress	$\Delta n/n$ (%)	$\Delta N/N$ (%)
G1	7.3 × 7.3 × 9.0	2.78	34	0.25	0.18	–	3.3	−28	–
G2	7.3 × 7.3 × 8.9	3.34	81	0.62	0.64	7.0	9.8	3	40
G3	7.3 × 7.3 × 8.8	3.87	79	0.32	3.61	17.0	9.5	1028	−44
L1	7.3 × 7.3 × 6.0	2.54	27	0.027	0.041[a]	3.0	4.5	52	50
L2	7.3 × 7.3 × 9.2	3.58	53	0.024	0.042[a]	2.6	3.8	75	48
L3	7.3 × 7.3 × 9.2	4.06	87	0.048	0.24[a]	7.6	46.4	500	509

The void density N in sample G1 could not be determined due to strong image noise.
[a] After compression small pieces of the samples L1–3 had splintered off the edges and the corresponding (artificially enlarged) void spaces were excluded by applying a size filter.

and shape; the latter is characterized by a sphericity factor F which is "1" for a sphere and <1 for any other object (cf. Appendix B). Obviously the voids in the limestone are smaller (Fig. 5b and d) and appear "rounder" than those present in the greywacke (Fig. 5a and c). Fig. 5d shows that the number of voids in L2 increases steadily towards $F = 1$ (value for a sphere). Comparison with high-resolution SEM pictures (Fig. 1c) shows that this result has to be taken carefully because ragged voids will be smoothed by the limited image resolution. In the samples G1–3 we find larger voids of irregular, non-spherical shape (Fig. 5c shows a peak at $F \sim 0.75$) and a significant amount of very small voids characterized by a second peak at $F = 1$. Note that sphericity is not a unique description of the shape of the voids. We therefore compared these quantitative results to 2D projection images of the entire void volume (Fig. 6). A binary image of the void volume (voids are represented by voxel values of "1" while the rest of the volume is set to "0") is projected numerically along one coordinate axis (x, y or z). A projection image of the voids in sample G2 is shown in

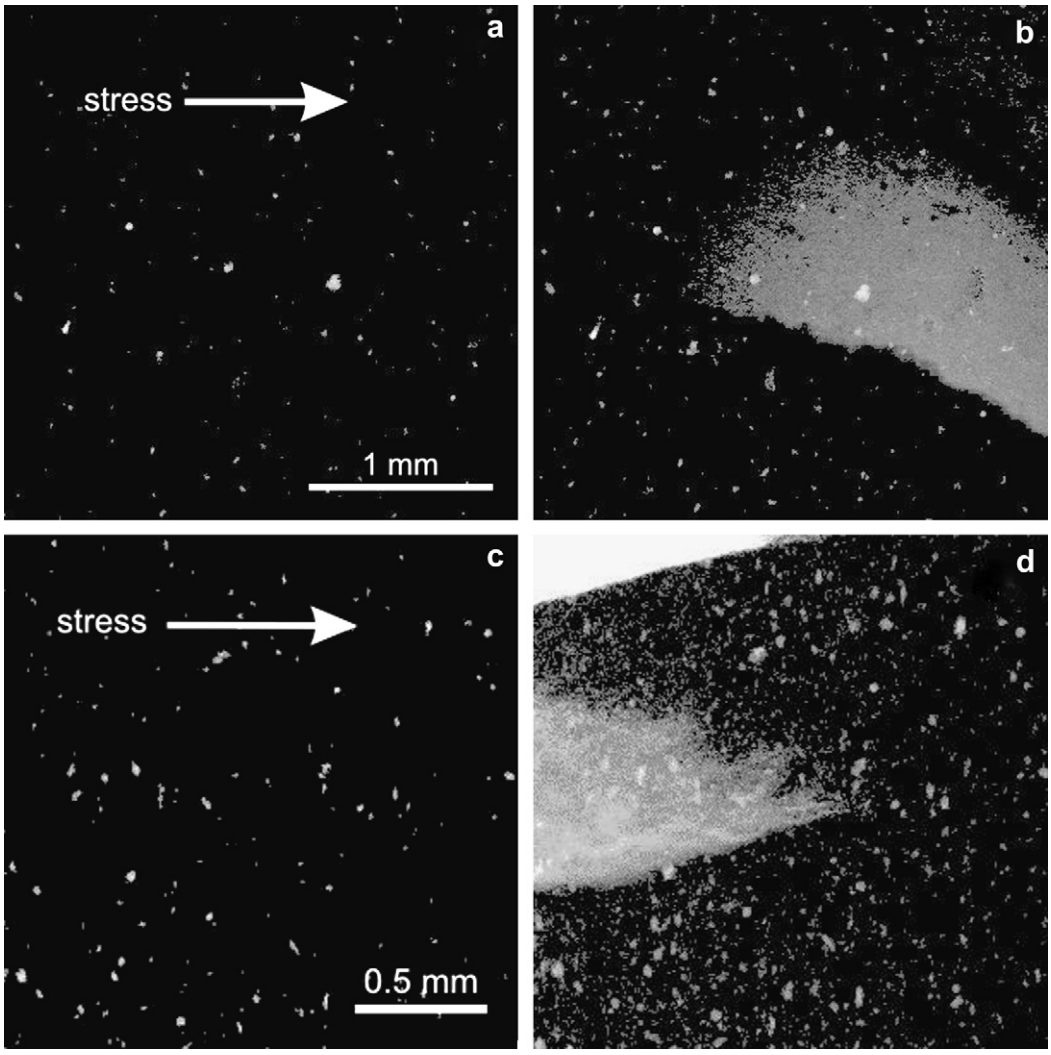

Fig. 4. Virtual projection of pores in a small section at the bottom of the sample L2 (a) before and (b) after deformation causing the formation of a small crack. Top edge of sample L3 (c) before and (d) after deformation and cracking.

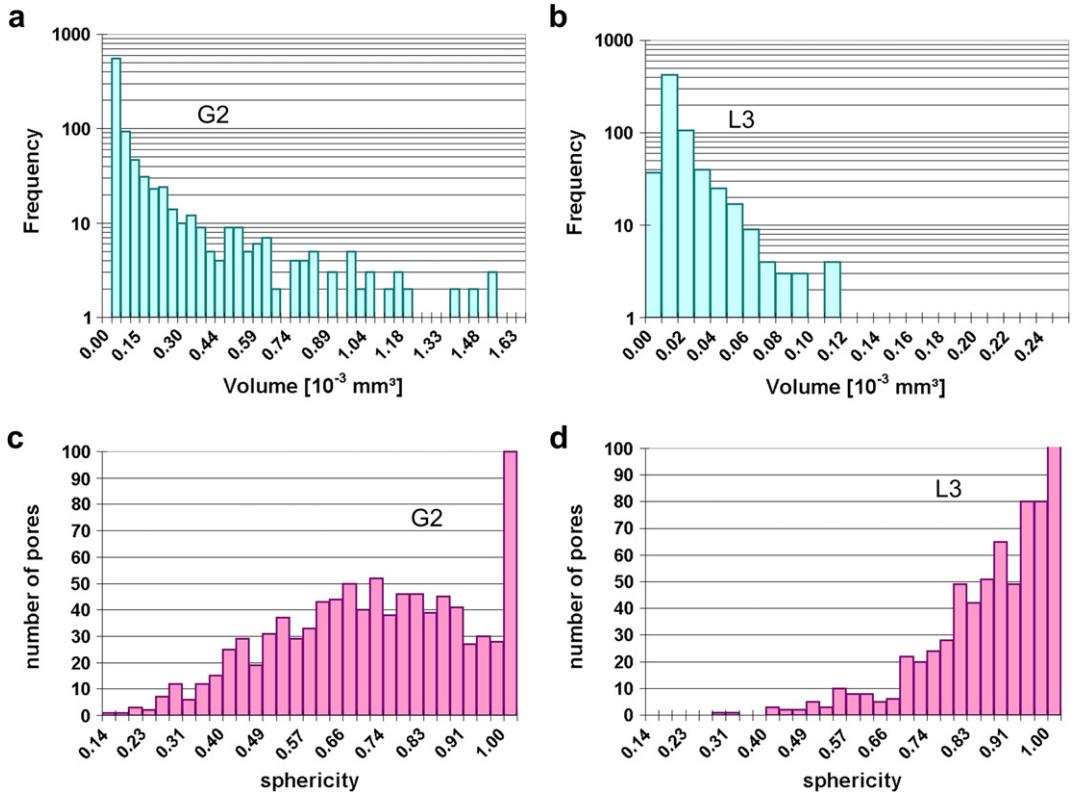

Fig. 5. (a,b) Histograms showing the distribution of pore volume in samples G2 (a) and L2 (b). (c,d) Distributions of pore shape (sphericity) calculated for G2 (c) and L2 (d). Note that a sphericity of "1" corresponds to a spherical pore.

Fig. 6a along with an enlarged view (Fig. 6b) revealing a large variety of pore sizes and shapes (the image lies in the x–z plane, the crack lies slightly obliquely to the y–z plane).

A lower part of the uncompressed greywacke sample G3 is shown as a sagital (top-to-bottom) slice through the image volume in Fig. 7a and may be interpreted in the same manner as a thin section. It may be clearly seen that the grain structure is typical of greywacke: poorly sorted angular grains of different minerals separated by a fine grained ground mass. After deformation at 90% of the average maximum strain, a macroscopic crack formed (Fig. 7b); the crack is wider at the top than at the bottom where it is difficult to see. The description of the components of the crack is shown in Fig. 7c: grain-boundary cracks, intrangranular cracks (dividing mineral grains), and cracks in the intergranular matrix. The component cracks traverse the sample in several orientations (Fig. 7d). In the upper half of the sample, there are tensile cracks sub-parallel to the applied stress. Further below, isolated tensile cracks appear connected by wing cracks splaying from the upper tensile cracks at an angle of approximately 45° to stress direction. In the lower part of Fig. 7c there is a crack which has coalesced from a number of cracks which are too small to be clearly imaged. At the lower end of the coalesced crack, a wing crack, oriented at 90° to the wing cracks in the upper part of the sample, has propagated through the matrix. Three small tensile cracks opened close to the lower end of the sample.

To investigate the relationship of the directions of the various crack components, a sagital slice along the entire sample perpendicular to the crack was selected. From this image, a binary image of the crack and a rose diagram of the crack components calculated from the binary image were made (Fig. 8). The crack developed at an angle of ca. 10° from the stress direction and appears to have a rather simple structure; however, the rose diagram shows the complexity of the interplay of the cracks generated by the uniaxial stress. Sub-micro-cracks in the stress direction (labeled tensile cracks) dominate the rose diagram; in addition there is a cluster of directions between 20° and 45° with 2 distinct peaks at 30° to 35° and at 40° to 45°. Also there is a well-defined peak at 325° to 330°. These sets of directions represent shear fractures (labeled wing cracks in Fig. 7d) which interconnect the tensile cracks.

In addition to this 2D "thin-section" analysis, the three-dimensional nature of the data permits a volumetric analysis of the crack, i.e., we may determine how crack thickness varies along the length of the crack (for details see Appendix C). In order to quantify its shape, total size and orientation, the macro-crack is binarized and separated from the smaller isolated voids in the sample volume. This procedure requires a special type of binarization based on a region-growth algorithm and the application of a size filter that grants survival only to the largest object in the sub-volume containing the crack. By counting the remaining voxels, a crack volume of 0.15 mm^3 was computed. In order to investigate the topography of the crack a plane was fitted to the crack (Fig. 9a). The normal vector to this "crack plane" coincides with the major inertia axis of the crack (see Appendix C). The crack "topography" (perpendicular crack surface-to-plane distance) is shown in Fig. 9b.

The standard deviation of the crack surface-to-plane distance equals $\pm 52\,\mu m$ and by comparing this value to the length ($\sim$8.6 mm along the direction of crack propagation) and width ($\sim$5.0 mm) of the crack, we may see that it is quasi-planar on the macroscopic scale. In order to visualize the local thickness of the crack we sum all crack voxels lying on a line perpendicular to the crack plane. The resulting thickness is projected onto the crack plane (Fig. 10a). This macro-crack has a wedge-shaped thickness profile along the direction of maximum compression with an opening of $\sim 100\,\mu m$ at the top and $\sim 7\,\mu m$ at the bottom indicating that nucleation occurred at the top. Small micro-cracks probably extend further into the sample but are not detected. Fig. 10a

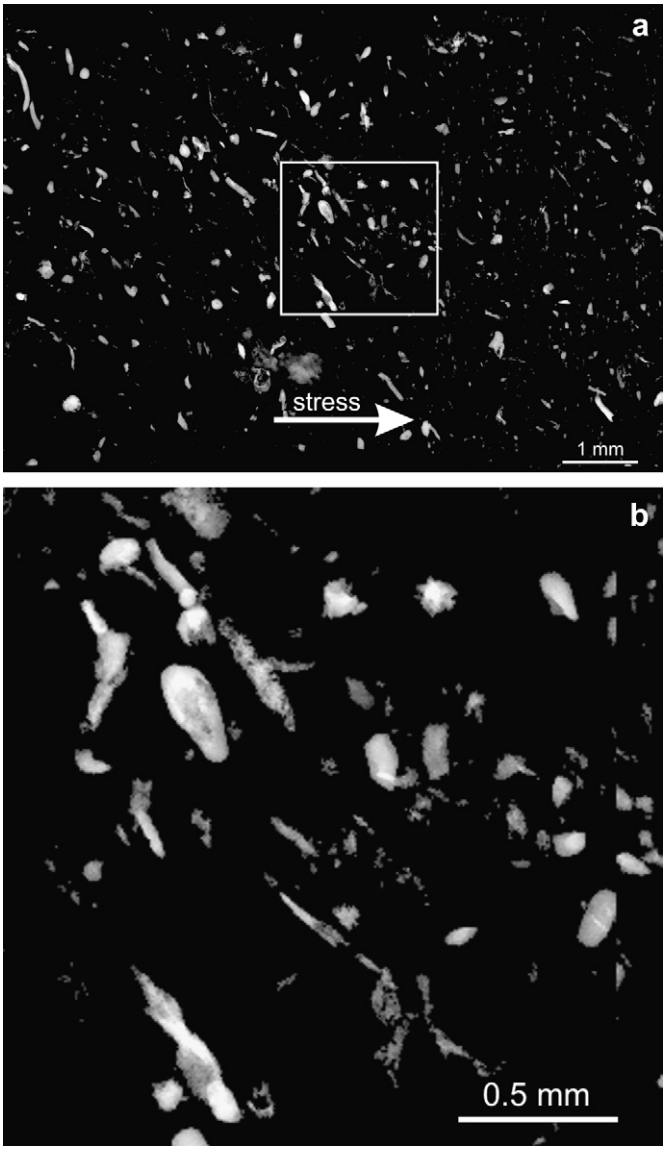

Fig. 6. (a) Virtual projection of the pore space in the sample G2. (b) The magnification reveals elongated pores that seem to follow a general orientation of the mineral. Randomly oriented oval and angular pores are observed as well.

contains a few image artifacts ("bright clouds", marked by arrows) caused by low density mineral grains that were partially connected to the crack and can thus not be fully separated from the latter by the binarization algorithm.

In order to analyze the mineral constituents in the area of crack propagation we combine the records of the sample G3 before and after compression. The two datasets are spatially aligned in the Euclidean coordinate system, and a box is cropped around the matching regions where the crack formed during deformation. Masking this region in the uncompressed sample with the binary image of the crack in the compressed sample yields a three-dimensional volume showing the mineral structure previous to fracturing. Projecting this data along lines perpendicular to the crack plane and normalizing the resulting image by division by the crack thickness (Fig. 10a) we obtain a map of the mineral constituents that were traversed by the crack (Fig. 10b). Dense ore minerals (bright) and less dense feldspars (dark) indicate where mineral grains were split by intra-granular micro-cracks. At the top of Fig. 10b where the fracture initiated (marked "B"), the fracture mainly traversed a fine inter-granular matrix (appearing more or less homogeneous in gray), whereas in other regions (marked "A" in Fig. 10b) larger feldspars were apparently split by tensile cracks. In the lower part (marked "C"), the fracture tip is mainly composed of inter-granular cracks, larger grains are not fractured (black).

We complete the analysis by showing projections of the total void space similar to Fig. 6 before and after formation of the macro-crack in sample G3 (Fig. 11a and b). The important conclusion from Fig. 11 is that the formation of the macroscopic crack (Fig. 11b) was not controlled by the pre-existing void spaces shown in Fig. 11a.

By contrast, in the limestone samples L2 and L3 somewhat smaller cracks formed after compression on the top and bottom sample edges respectively (Fig. 4a and b). The crack in L2 is approx. 2.0×1.0 mm in size and shows a very ragged shape except where it runs along the cylinder surface. The topography is quasi-planar and tilted by approx. 8° with respect to the direction of maximum compression. The crack in sample L3 is even smaller (approx. 1.2×0.6 mm) with a similar orientation. Because of the small size of the cracks, it was not possible to decompose these cracks into tensile and wing cracks for further analysis.

6. Discussion

In this work high-resolution X-ray tomography was applied to small cylinders of limestone and greywacke. The tomography was carried out before deformation to characterize grain types and sizes and the presence of voids. Statistical analysis of the void space in samples G2 and L2 showed voids of various sizes and shapes in the greywacke and small round pores in the limestone. Electron microscopy revealed the latter to be part of a larger network of intergranular porosity which is not imaged due to the limited spatial resolution of the X-ray detector system. It is important to note that values for the total void space in these materials, which are found in the literature and are measured by other methods (e.g., mercury intrusion or scanning electron microscopy), indicate a larger void space than that which we calculated from the tomographic data. A reasonable explanation for this discrepancy is that an important part of the void space is smaller than the detection limit of our method, i.e. smaller than 10 μm in size. In addition very large voids (mm- or even cm-sized) were excluded because of the small sample sizes which were taken preferentially from homogeneous and compact regions in the rock.

The tomography experiments were carried out at 60%, 80% and 90% of the maximum average strain to define how the sample reacted to progressively greater stress. As the uniaxial compressive stress increased, changes in void space as well as crack development were observed. The strongly heterogeneous composition of the greywacke and the fine homogeneous micro-structure of limestone led to quite different behavior of these two materials when stressed. At 60% maximum average strain, the greywacke sample G1 showed a reduction in void space ($\Delta n/n = -28\%$ for G1, Table 1). At 80% maximum average strain, sample G2 exhibited relatively small increases in void volume ($\Delta n/n = 3\%$). On the other hand, in the limestone samples, which had initial values of void space and void density lower by a factor of 10 than those of the greywacke, the increases were somewhat greater ($\Delta n/n = 52\%$ in L1 and $\Delta n/n = 75\%$ in L2, see Table 1). Thus, after initial closure of voids in G1, the void space and density in both sets of samples increased with higher stress. The greywacke perhaps was more resistant to compression than the limestone. At 90% of the maximum average strain, the greywacke sample G3 showed more than 1000% increase in void space with a decreasing void density, both effects may be attributed to the generation of the "macro-crack". Deformation of sample L3 reveals a different picture, where a strong increase in void volume is accompanied by an increasing void density. One might see a weak correlation between the orientation of the macroscopic crack in the deformed sample G3 and numerous dense

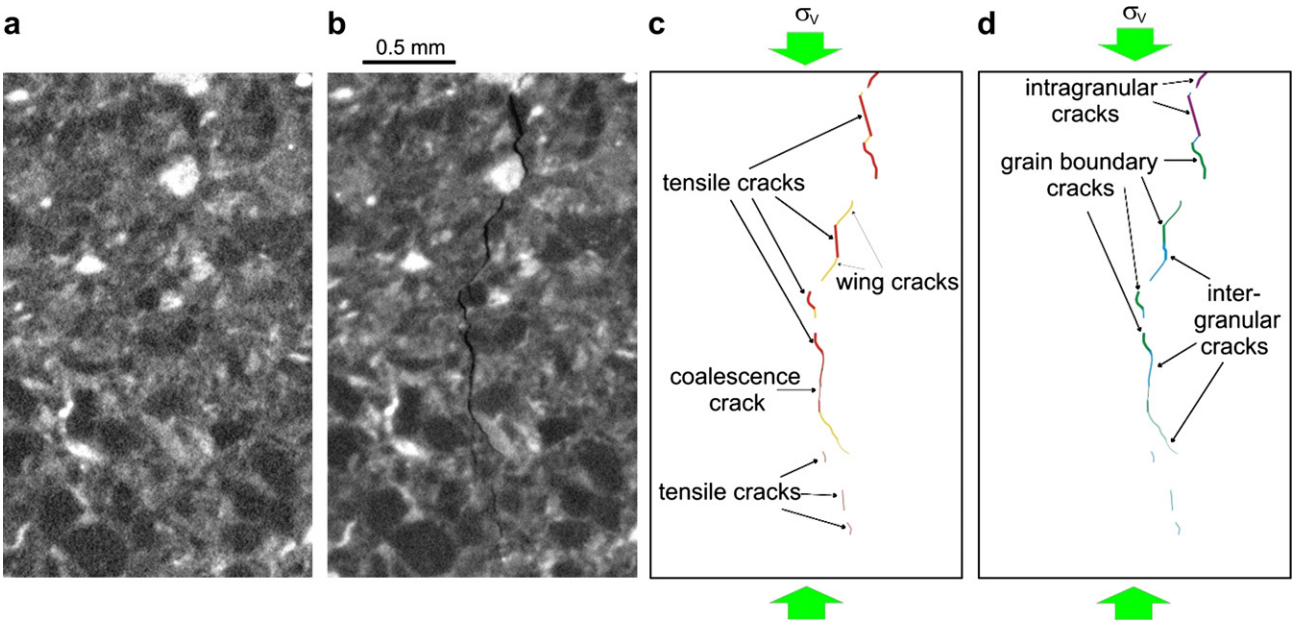

Fig. 7. Sagital slice through the 3D data (a) before and (b) after deformation/formation of a macro-crack in sample G3. (c) The macro-crack is decomposed into tensile cracks, parallel to the deformation, oblique wing-cracks and coalescence cracks. Cracks run through (intra-granular), alongside (grain-boundary) or between grains (inter-granular).

iron-oxide-filled spaces (associated with an old "healed" crack) in the same sample. Although their orientation with respect to the stress direction differs (30° for the old, 10° for the new crack) and they lie on opposite sides of the sample cylinder they seems to have a tendency to align (the normal vectors of the two planes "only" spread by ~20°) which may indicate that the material has a preferred orientation for cracking. Further tests (data not shown) indicate that new cracks in the greywacke are most likely to open up old healed cracks when the latter align well with the direction of applied stress. The fracture observed in Fig. 2b is apparently an exception where an old crack that is inclined 30° to the direction of stress is re-opened by the new fracture whereas in general these two would not align (e.g. sample G3).

One of the unknowns in fracture mechanics is "where does a crack originate?". It is generally agreed that the "how" is that an initial micro-crack opens due to tensile stresses. In modeling crack behavior, penny-shaped micro-cracks distributed throughout the model are most commonly used to represent the initial flaws in brittle materials (e.g., Adams and Sines, 1978; Cannon et al., 1990; Dyskin et al., 2003; Germanovich et al., 1994; Healy et al., 2006). At the onset of brittle fracture, a process zone of circular shape (when extrapolated from 2D sections, cf. Atkinson, 1987) is associated with the non-linear behavior of crack tips. This process is further refined by Healy et al. (2006) who state "Elastic stress in 3 dimensions around tensile micro-cracks promotes a mutual interaction that produces brittle shear planes oriented obliquely to the remote principal stresses". However, the modeling process does not tell us where or why in nature cracks choose to originate.

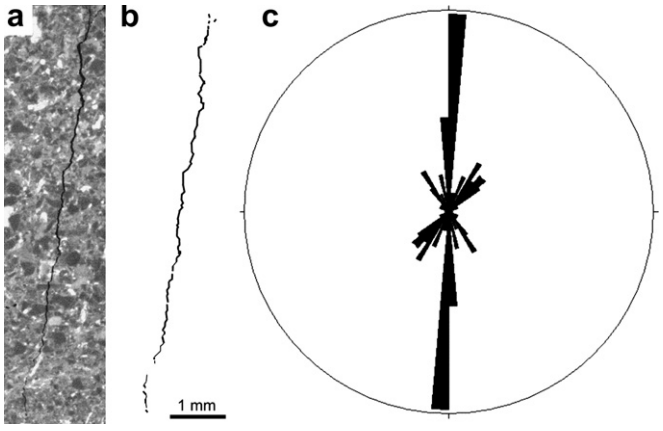

Fig. 8. 2D orientation analysis of the macro-crack in sample G3. (a) Sagital slice (perpendicularly to the crack plane and parallel to the crack propagation) showing the complete crack. (b) Binary image of the crack. (c) Rose diagram of crack orientation.

Our observations from the undeformed greywacke samples reveal voids of various shapes, sizes, and orientations that do not correlate with crack propagation in sample G3 (Figs. 6, 7). The kinks in the stress–strain curves from the fracture tests on greywacke and limestone (Fig. 2) indicate that initial cracking occurred but was followed by further elastic deformation before brittle failure. This behavior may be an artifact of the sample dimensions. An image of the micro-structure of sample G3 in its undeformed state is shown in Fig. 10b and reveals where and how the crack developed in the sample. The crack initially formed at the upper surface of the sample in an area of fine-grained intergranular material with particularly low void space (Fig. 11). However, this statement applies to only voids of 10 μm size or larger. Smaller voids (<10 μm) could be the locus of the initial cracking (e.g. numerous micrometer-sized voids were observed in SEM images of the grain boundaries in the greywacke and limestone). The crack propagated along grain boundaries, through mineral grains, probably along cleavage planes, and the fine intergranular matrix almost to the bottom surface of the sample (Figs. 7, 8, and 11). An image of the undeformed micro-structure that was traversed by the crack does not appear much different from an arbitrary cross-section through the material. As can be seen in Figs. 9, 10 and 11b coalesced or isolated micro-cracks are located in the plane of the crack and at the tip of the propagating crack. In Figs. 7 and 8 it may be seen that the angle the macro-crack makes with the stress direction (~10°) results from the interplay of parallel tensile cracks and oblique wing cracks. At the tip of the macro-crack some individual micro-cracks are observed (Figs. 7 and 11b). From the 2D slice in Fig. 7, we may interpret a kinematic sequence whereby cracking begins at a point

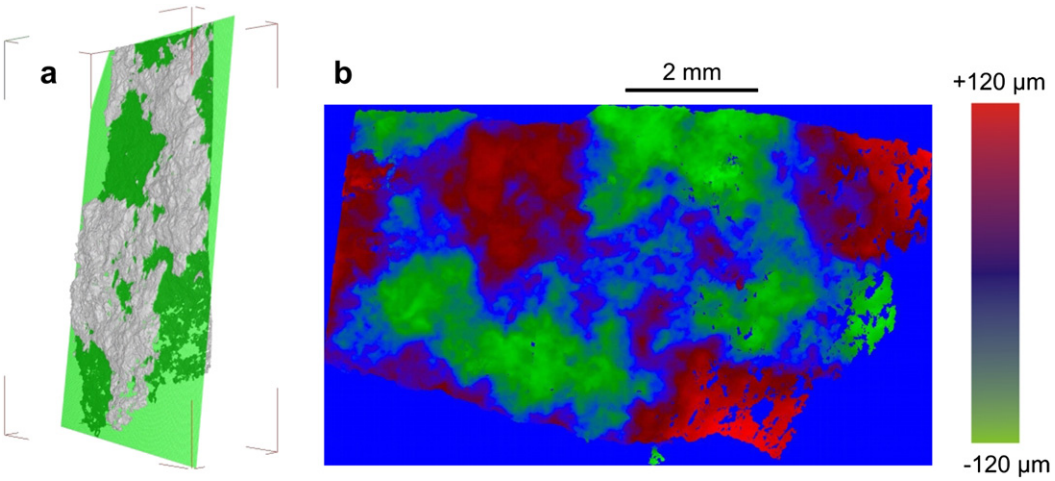

Fig. 9. (a) The quasi-planar macro-crack is projected onto the plane perpendicular to its major orientation axis. (b) A "topography" view is calculated from the distance of each voxel (belonging to the crack) normal to the plane (red, above; green, below the plane).

and propagation and growth occur via interaction between tensile and shear cracks. Similar behavior of fracture initiation and growth was shown using AE (Reches and Lockner, 1994; Lei et al., 2000).

Compared to the greywacke, the formation of cracks in limestone takes place on a smaller scale (see Fig. 4) in accordance with the very fine grains that characterize the micro-structure of this material. We observed a systematic increase in the limestone porosity after compression and from these observations one could hypothesize that the deformation energy applied to limestone yields the formation of new micro-voids preceding the formation of larger cracks. Our data shows that the typical multi-columnar fracture of the limestone samples starts at the cylinder's vertical surface with millimeter-sized cracks preceding the spalling of small splinters.

7. Conclusions

We have shown that high resolution X-ray tomography is a superior method to investigate the behavior of rock samples under uniaxial compression. This method generates a 3D image of the sample before compression which can be compared with the same sample after brittle failure. The 3D image allows the sample to be

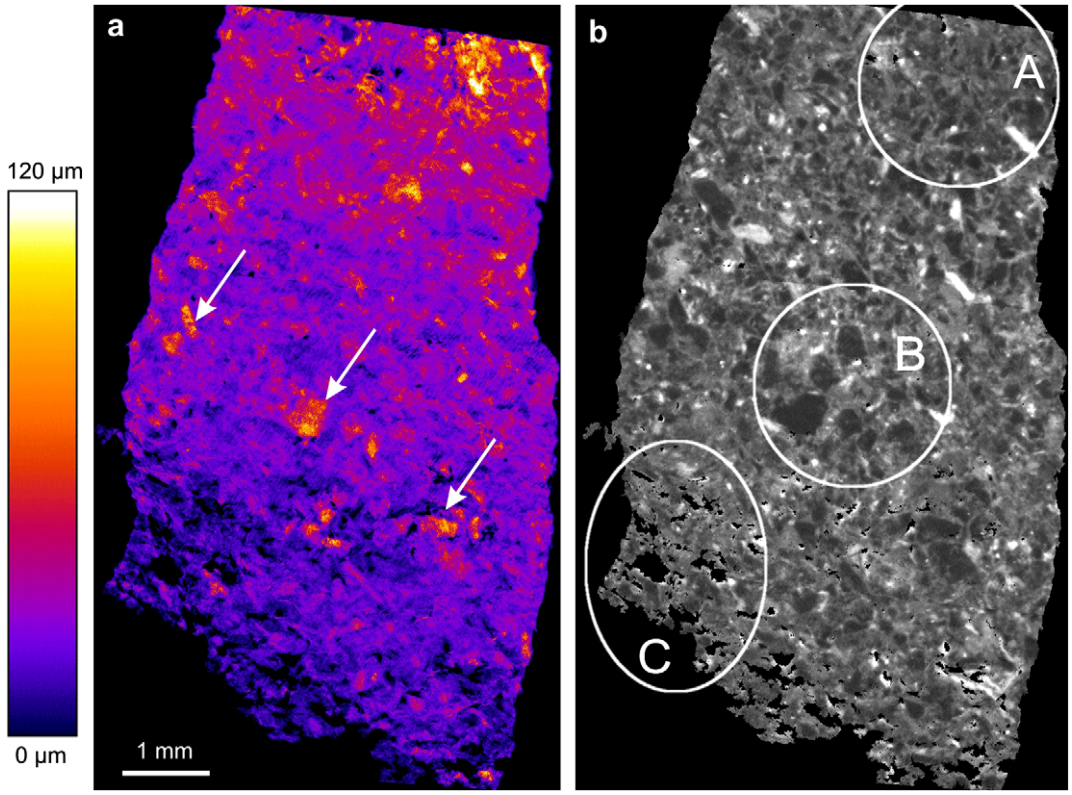

Fig. 10. (a) The thickness of the crack is projected onto the crack plane. Some artifacts appear (white arrows) due to mineral particles of low density (dark appearance in (b)) that are artificially counted as pores. (b) The projected map of the G3 micro-structure in its undeformed state masked by the binary crack image of the matching structure after deformation and normalized by the crack thickness (A, region of inter-granular cracks; B, intra-granular cracks; and C, grains that appear to be spared by the fracture).

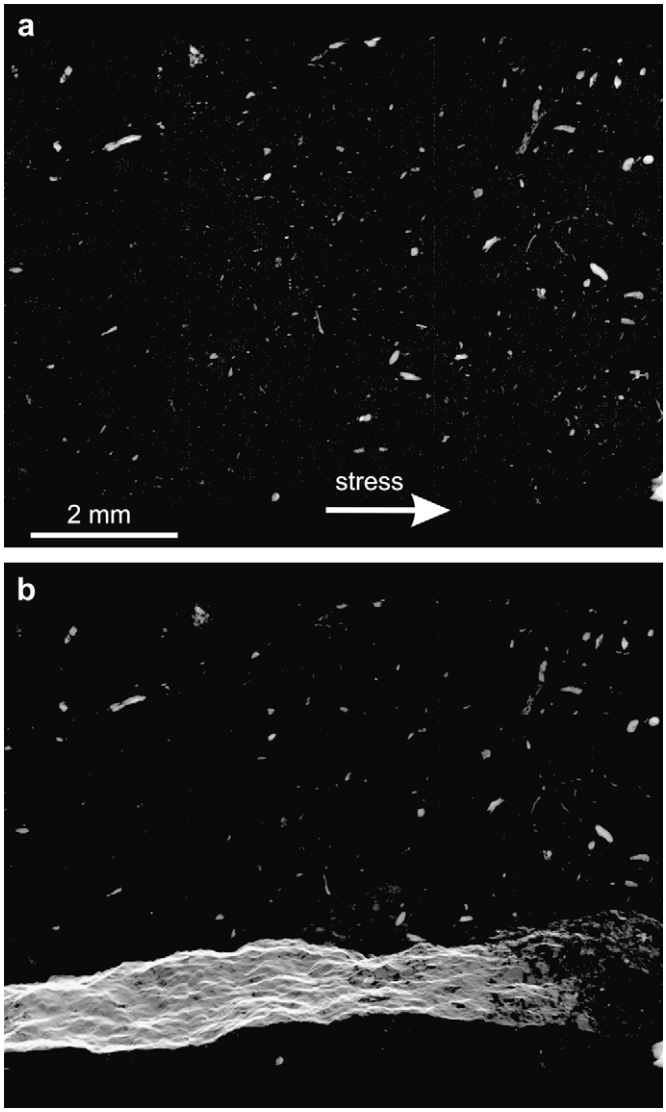

Fig. 11. Virtual projection of the pores in the third greywacke sample before (a) and after (b) uniaxial compression causing formation of a macroscopic crack. It can be seen from (b) that crack formation and propagation occurred independently of the pre-existing porosity distribution in the sample.

viewed from all perspectives and as many cross-sections as wished may be analyzed and compared with the results from other methods, e.g., thin or polished sections. With further development the method will permit deeper insights into rock fracturing. From our experimental results, we conclude that the crack initiated in fine-grained material; the locus of initiation was not defined by the tomography. The principal sites for the macro-crack propagation in the greywacke are the grain-boundaries defined by the imaging before compression. None of the voids which were imaged by the method were involved in the initiation of the macro-crack. Within the resolution limits of the chosen imaging system we may exclude the case where pre-existing void space would localize the zone of crack initiation. The image of the macro-crack in sample G3 showed that it may have been formed through the creation of new tensile cracks which were later linked by wing cracks of different orientations and propagated from the upper surface of the sample to within a few millimeters of the lower surface. None of the fractures were created by the re-activation of pre-existing cracks; they are all newly formed. We assume that crack growth in limestone samples took place in a similar manner. To investigate the local microstructure through which the crack propagation took place, it will be necessary to carry out the tomography studies with a spatial resolution higher than the 10 μm used in this study.

Our findings are in good agreement with common fracture kinematics where cracks ranging from centimeters to a few kilometers are considered and the fracture process zone extends at least over a few tens of mm. Note that the "macro-crack" we characterized in the greywacke sample is closer in size to what is commonly called a "micro-crack" (referring to its thickness).

In contrast to planar imaging methods, X-ray tomography data allows for direct interpretation of fracturing, and quantitative analysis of the fractures can be performed using 3D image analysis. The method's principal strength is that the sample may be imaged non-destructively before compression testing, its only drawback, depending on the grain size of the sample, is that sample size is limited. This study has demonstrated the effectiveness of this method and its application to other types of rock should create more insights into crack formation and rock deformation. We think that high resolution tomography because of its ability to non-destructively image rock samples will contribute substantially to the understanding of brittle rock deformation.

Acknowledgements

We thank Dr P. Zaslansky for his help and the very fruitful discussions concerning this work. Our gratitude goes to Dr J. Goebbels, Dr G. Weidemann and T. Wolk for their support during experiments at BESSY. We further want to acknowledge the extensive work of the Journal reviewers whose comments and suggestions helped us to improve this article.

Appendix A. synchrotron microtomography

Compared to modern laboratory CT this method has many advantages: (1) transmission and projection of the beam take place in a quasi-parallel geometry thus simplifying the numerical reconstruction of the volume images (filtered back-projection) while minimizing imaging artifacts; (2) powerful X-ray sources (insertion devices) can be used to create an extremely high photon flux making the exclusive use of a quasi-monochromatic energy band possible; and (3) high-resolution data is reconstructed from projection images recorded over a 180° interval within a reasonable time frame of approximately 1 h. In addition monochromatic X-ray tomography is free of imaging artifacts that are inherent in polychromatic lab-CT. In contrast to the widely used cone beam tomography, spatial resolution in parallel beam imaging is limited only by the X-ray detector (scintillator screen), not by the size of the source. This makes synchrotrons an ideal place for high-resolution micro-CT applications (Bonse and Busch, 1996).

The measurements described above were performed on the BAM*line* at the Berlin electron storage ring BESSY (Görner et al., 2001; Rack et al., 2008). This experimental station is situated 35 m downstream of a 7 T wavelength shifter (WLS). The WLS generates hard X-rays from 6 keV up to 80 keV by modulating the trajectory of electrons circulating in the storage ring. Two multilayer mirrors act as a band pass filter to provide quasi-monochromatic irradiation with a sufficient photon flux and a monochromaticity of approx. $\Delta E/E = 10^{-2}$. X-rays with photon energy of 33 keV were used for all reported measurements. Sample rotation of 180° was performed in incremental steps of 0.2° and brightfield images (with the sample moved off the beam) were recorded every 100 projections in order to correct for decreasing beam intensity due to the loss of electron current as well as for fluctuations of the inhomogeneous X-ray illumination. The sample is fixed onto a motorized stage allowing micrometer-precise positioning and rotation with respect to the detector screen. The detector is placed behind the sample along the

axis of the incoming X-rays and comprises three main elements: a scintillator screen, magnifying optics and a CCD camera. First the X-rays impinge onto quartz glass coated with a 10 μm thick layer of Gd_2O_2S (Gadox) powder. The luminescent picture of the transmitted beam is then magnified by the combination of a Rodenstock TV-Heliflex (1:1.1, $f = 50$ mm) objective and a Nikkor telephoto ($f = 180$ mm/2.8 ED). Finally the magnified image is recorded by a Princeton Instruments VersArray 2048B back-illuminated CCD camera. This setup provides an effective pixel size of 3.6 μm (resolution ~10 μm) with a squared field of view of ca. 7.2 mm length.

Appendix B. Analysis of the micro-void volume

In this work the data analysis is focused on the void space inside the rocks. Voids can easily be discerned from the solid particles because they are represented by the darkest voxels in the microstructure due to negligible X-ray absorption. Using 3D image analysis tools the structure is binarized, with the pore voxels defined as *foreground* (voxels are set to "1") and the rest of the sample voxels forming the *background* (voxels are set to "0"). From these binary datasets we calculated the position, shape and volume of each void in the sample. Concerning the void volume a cutoff was applied to eliminate voids smaller that 10 voxels in size, in order to avoid pixel noise which could be interpreted as voids. In addition to the voids, very dense particles were selected and analyzed in greywacke (iron oxides, see Fig. 4c) and limestone (pyrites). In order to correct for the remaining uncertainty about the pore binarization thresholds, we used the total volume of these dense minerals (which is supposed to be invariant to deformation) for normalizing the total porosity and pore density before and after deformation. In order to describe the shape of the voids a sphericity factor F was calculated:

$$F = 6\sqrt{\pi}\frac{V}{\sqrt{S^3}} \tag{1}$$

where V is the void volume, S the void surface and $F = 1$ for a sphere and $F < 1$ otherwise.

Appendix C. Orientation analysis of the macro-crack

In order to calculate shape and orientation of the macro-crack we compute its inertia tensor using the formula:

$$J_{ij} = \sum_{\vec{x} \subset \text{crack}} m(\vec{x}) \cdot x_i x_j \tag{2}$$

where $x = (x_1, x_2, x_3)^{\mathrm{T}}$; x is the coordinate vector relative to the centre of mass of all crack voxels in the framework of the reconstructed tomogram and the mass $m(\vec{x})$ of the voxel x. Because we are looking at a void space, a virtual mass $m = 1$ is associated with all voxels and J_{ij} becomes the orientation tensor T_{ij} from which we can obtain the eigenvalues λ_i and eigenvectors $\vec{t_i}$. T is symmetric ($T_{ab} = T_{ba}$) and therefore the eigenvalues are real and the eigenvectors span an orthogonal basis in Euclidian space. The transformation matrix $A^{-1} = \{\vec{t_1}, \vec{t_2}, \vec{t_3}\}^{-1}$ is also orthogonal ($A^{-1} = A^{\mathrm{T}}$) and can be calculated directly from the eigenvectors. To fit the entire crack to a plane we apply a coordinate transformation and calculate $\vec{\xi} = (\xi_1, \xi_2, \xi_3) = A^{\mathrm{T}} \cdot \vec{x}$ with ξ_1 and ξ_2 the new coordinates in the crack plane and ξ_3 the distance of the crack voxel x normal to the fitting plane.

References

Adams, M., Sines, G., 1978. Crack extension from flaws in a brittle material subjected to compression. Tectonophysics 49, 97–118.

Atkinson, B.K. (Ed.), 1987. Fracture Mechanics of Rock. Academic Press, London.

Bastuerk, M., Bichler, M., Dlouhy, A., Tatlisu, H., Zamani, B., Zawisky, M., 2004. Application of Neutron Radiography in Aerospace Industry and Geology. 16th World Conference on Nondestructive Testing, Montreal, Canada, NDT.net.

Bésuelle, P., Viggiani, G., Lenoir, N., Desrues, J., Bornert, M., 2006. X-ray micro CT for studying strain localization in clay rocks under triaxial compression. In: Desrues, J., Viggiani, G., Bésuelle, P. (Eds.), Advances in X-ray Tomography for Geomaterials. Antony Rowe Ltd., Chippenham, Wiltshire, pp. 35–52.

Bieniawski, Z.T., 1967. Mechanism of brittle fracture of rock part II – experimental studies. International Journal of Rock Mechanics and Mining Sciences 4, 407–423.

Bobet, A., Einstein, H.H., 1998. Fracture coalescence in rock-type materials under uniaxial and biaxial compression. International Journal of Rock Mechanics and Mining Sciences 35, 863–888.

Bonse, U., Busch, F., 1996. X-ray computed microtomography (μCT) using synchrotron radiation (SR). Progress in Biophysics and Molecular Biology 65 (1/2), 133–169.

Cannon, N.P., Schulson, E.M., Smith, T.R., Frost, H.J., 1990. Wing cracks and brittle compressive fracture. Acta Metallurgica Materialia 38, 1955–1962.

Desrues, J., Viggiani, G., Bésuelle, P. (Eds.), 2006. Advances in X-ray Tomography for Geomaterials. Antony Rowe Ltd., Chippenham, Wiltshire, p. 452.

Dyskin, A.V., Germanovich, L.N., Jewell, R.J., Joer, H., Krasinski, J.S., Lee, K.K., Roegiers, J.-C., Sahouryeh, E., Ustinov, K.B., 1995. Some experimental results on three-dimensional crack propagation in compression. In: Rossmanith, H.-P. (Ed.), Mechanics of Jointed and Faulted Rock. Balkema, Rotterdam, pp. 91–96.

Dyskin, A.V., Sahouryeh, E., Jewell, R.J., Joer, H., Ustinov, K.B., 2003. Influence of shape and locations of initial 3-D cracks on their growth in uniaxial compression. Engineering Fracture Mechanics 70, 2115–2136.

Fredrich, J.T., Menéndez, B., Wong, T.-F., 1995. Imaging the pore structure of geomaterials. Science 268, 276–279.

Germanovich, L.N., Salganik, R.L., Dyskin, A.V., Lee, K.K., 1994. Mechanisms of brittle fracture of rock with pre-existing cracks in compression. Pure and Applied Geophysics 143, 117–149.

Görner, W., Hentschel, M.P., Müller, B.R., Riesemeier, H., Krumrey, M., Ulm, G., Diete, W., Klein, U., Frahm, R., 2001. BAMline: the first hard X-ray beamline at BESSY II. Nuclear Instruments and Methods in Physics Research Section A 467-468, 703–706.

Griffith, A.A., 1920. The phenomena of rupture and flow in solids. Philosophical Transactions of the Royal Society of London, Series A 221, 163–198.

Griffith, A.A., 1924. The Theory of Rupture. 1st International Congress on Applied Mechanics, Delft.

Healy, D., Jones, R.R., Holdsworth, R.E., 2006. Three-dimensional brittle shear fracturing by tensile crack interaction. Nature 439, 64–67.

Hirono, T., Takahashi, M., Nakashima, S., 2003. In situ visualization of fluid flow image within deformed rock by X-ray CT. Engineering Geology 70, 37–46.

Hoek, E., Bieniawski, Z.T., 1965. Brittle fracture propagation in rock under compression. International Journal of Fracture Mechanics 1, 137–155.

Horii, H., Nemat-Nasser, S., 1985. Compression-induced microcrack growth in brittle solids: axial splitting and shear failure. Journal of Geophysical Research 90 (B4), 3105–3125.

Janssen, C., Wagner, F.C., Zang, A., Dresen, G.F., 2001. Fracture process zone in granite: a microstructural analysis. International Journal of Earth Sciences 90, 46–59.

Ketcham, R., 2005. Three-dimensional grain fabric measurements using high-resolution X-ray computed tomography. Journal of Structural Geology 27, 1217–1228.

Kranz, R.L., 1983. Microcracks in rocks: a review. Tectonophysics 100, 449–480.

Lajtai, E.Z., 1971. A theoretical and experimental evaluation of the Griffith theory of brittle fracture. Tectonophysics 11, 129–156.

Lajtai, E.Z., 1974. Brittle fracture in compression. International Journal of Fracture 10, 525–536.

Landis, E.N., 2006. X-ray tomography as a tool for micromechanical investigations of cement and mortar. In: Desrues, J., Viggiani, G., Bésuelle, P. (Eds.), Advances in X-ray Tomography for Geomaterials. Antony Rowe Ltd., Chippenham, Wiltshire, pp. 79–93.

Landis, E.N., Nagy, E.N., Keane, D.T., 2003. Microstructure and fracture in three dimensions. Engineering Fracture Mechanics 70, 911–925.

Lei, X., Kusunose, K., Rao, M.V.M.S., Nishizawa, O., Satoh, T., 2000. Quasi-static fault growth and cracking in homogeneous brittle rock under triaxial compression using acoustic emission monitoring. Journal of Geophysical Research 105, 6127–6139.

Lenoir, N., Marello, S., Viggiani, G., Besuelle, P., Desrues, J., Di Michiel, M., 2003. X-ray micro tomography characterization of strain localization upon deviatoric loading of saturated fine-grained stiff soils. In: Otani, J., Obara, Y. (Eds.), X-ray CT for Geomaterials. A.A. Balkema Publishers, Kumamoto, Japan, pp. 147–155.

Lunati, I., Vontobel, P., Kinzelbach, W., Lehmann, E., 2003. Laboratory visualization of two-phase flow in a natural fracture by neutron tomography. Groundwater in Fractured Rocks. UNESCO IHP-VI, Series on Groundwater, Prague, Czech Republic.

Matsushima, T., Saomoto, H., Uesugi, K., Tsuchiyama, A., Nakano, T., 2003. Detection of 3-D irregular grain shape of Toyoura sand at SPring-8. In: Otani, J., Obara, Y. (Eds.), X-ray CT for Geomaterials. A.A. Balkema Publishers, Kumamoto, Japan, pp. 121–126.

McClintock, F.A., Walsh, J.B., 1962. Friction in Griffith cracks in rock under pressure. In: Proceedings of the 4th U.S. National Congress on Applied Mechanics, Vol. II. American Society of Mechanical Engineers, New York, pp. 1015–1021.

Moore, D.E., Lockner, D.A., 1995. The role of microcracking in shear-fracture propagation in granite. Journal of Structural Geology 17 (1), 95–114.
Nakashima, Y., Nakano, T., Nakamura, K., Uesugi, K., Tsuchiyama, A., Ikeda, S., 2004. Three-dimensional diffusion of non-sorbing species in porous sandstone: computer simulation based on X-ray microtomography using synchrotron radiation. Journal of Contaminant Hydrology 74, 253–264.
Ohtani, T., Nakano, T., Nakashima, Y., Muraoka, H., 2001. Three-dimensional shape analysis of miarolitic cavities and enclaves in the Kokkonda granite by X-ray computed tomography. Journal of Structural Geology 23, 1741–1751.
Otani, J., Obara, Y. (Eds.), 2003. X-ray CT for Geomaterials – Soils, Concrete, Rocks. International Workshop on X-ray CT for Geomaterials, November 6–7. A.A. Balkema Publishers, Kumamoto, Japan.
Pells, P.J.N., 1993. Uniaxial Strength Testing. Comprehensive Rock Engineering: Principles Practice and Projects. J.A. Hudson. 67–85.
Rack, A., Zabler, S., Mueller, B.R., Riesemeier, H., Weidemann, G., Lange, A., Goebbels, J., Hentschel, M., Goerner, W., 2008. High resolution synchrotron-based radiography and tomography using hard X-rays at the BAMline (BESSY II). Nuclear Instruments and Methods in Physics Research A 586 (2), 327–344.
Reches, Z., Lockner, D.A., 1994. Nucleation and growth of faults in brittle rocks. Journal of Geophysical Research 99 (B9), 18159–18173.
Scholz, C.H., 1990. The Mechanics of Earthquakes and Faulting. Cambridge University Press, New York, 439 pp.
Scholz, C.H., 2002. The Mechanics of Earthquakes and Faulting, second ed. Cambridge University Press, New York, 496 pp.
Schulson, E.M., Iliescu, D., Renshaw, C.E., 1999. On the initiation of shear faults during brittle compressive failure: a new mechanism. Journal of Geophysical Research 104 (B1), 695–705.
Vervoort, A., Wevers, M., Swennen, R., Roels, S., Van Geet, M., Sellers, E., 2003. Recent advantages of X-ray CT and its applications for rock material. In: Otani, J., Obara, Y. (Eds.), X-ray CT for Geomaterials. A.A. Balkema Publishers, Kumamoto, Japan, pp. 79–91.
Winkler, B., Knorr, K., Kahle, A., Vontobel, P., Lehmann, E., Hennion, B., Bayon, G., 2002. Neutron imaging an neutron tomography as non-destructive tools to study bulk-rock samples. European Journal of Mineralogy 14, 349–354.
Zang, A., Wagner, F.C., Stanchits, S., Janssen, C., Dresen, G., 2000. Fracture process zone in granite. Journal of Geophysical Research 105 (B10), 23651–23661.